Materials Today Bio 15 (2022) 100308

Contents lists available at ScienceDirect

Materials Today Bio

journal homepage: www.journals.elsevier.com/materials-today-bio

Glucose/ROS cascade-responsive ceria nanozymes for diabetic wound healing

Xiaojuan Yu [1], Xiaoxue Fu [1], Jiaxin Yang, Lu Chen, Feng Leng, Zhangyou Yang [*], Chao Yu [**]

Chongqing Key Laboratory for Pharmaceutical Metabolism Research, Chongqing Pharmacodynamic Evaluation Engineering Technology Research Center, College of Pharmacy, Chongqing Medical University, Chongqing, 400016, PR China

ARTICLE INFO

Keywords:
Coassembly
Cascade-responsive
Hyperglycemia
ROS-Scavenging
Diabetic wound

ABSTRACT

Diabetic wounds have an extremely complex microenvironment of hyperglycemia, hypoxia and high reactive oxygen species (ROS). Therefore, the regulation and management of this microenvironment may provide a new and improved treatment method for chronic diabetic wound healing. Herein, a glucose/ROS cascade-responsive nanozyme (CHA@GOx) was developed for diabetic wound treatment based on Ce-driven coassembly by a special dual ligand (alendronic acid and 2-methylimidazole) and glucose oxidase (GOx). It possesses superoxide dismutase and catalase mimic activities, which effectively remove excess ROS. In particular, it can catalyze excessive hydrogen peroxide generated by the glucose oxidation reaction to produce oxygen, regulate the oxygen balance of the wound, and reduce the toxic side effects of GOx, thus achieving the purpose of synergistically repairing diabetic wounds. *In vitro* experiments show that CHA@GOx assists mouse fibroblast migration and promotes human umbilical vein endothelial cell tube formation. *In vivo*, it can induce angiogenesis, collagen deposition, and re-epithelialization during wound healing in diabetic mice. Taken together, this study indicates that the coassembly of multifunctional nanozymes has implications in diabetic wound healing.

1. Introduction

Diabetes is one of the major threats to human health [1,2]. Among its multiple complications, diabetic wounds are of concern and pose a heavy medical burden due to their intractability [3]. The key reason for the slow healing of diabetic wounds is the poor wound microenvironment, which is often hyperglycemic [4,5], hypoxic [6–8] and accompanied by high levels of reactive oxygen species (ROS) [9–12]. It is important to note that these adverse factors are not independent of each other. For example, persistent high glucose disrupts the integrity of the cell lining associated with skin healing, making cells more susceptible to isolation and apoptosis [13], while leukocytes, neutrophils and macrophages will be less attracted to the site of injury, where their role is to eliminate cellular debris or bacteria from the wound site during the early stages of wound healing [14,15]. In addition, secretion of proangiogenic cytokines such as vascular endothelial growth factor and platelet-derived growth factor will be reduced, resulting in further impediment of angiogenesis that sustains cell growth and nutrient supply [16]. At the same time, massive glucose oxidation increases oxygen consumption, exacerbating intracellular hypoxia and ROS formation [17]. The proliferation and migration of important cells involved in wound healing (e.g., fibroblasts [18], vascular cells [10], etc.) are reduced under these conditions, ultimately impeding wound repair. Current research favors accelerating diabetic wound healing through drug delivery [19,20], 3D printing materials and patches [21,22] etc. for continuous oxygenation [23], removal of excess ROS [24], antibacterial [25–27], and promotion of vascular regeneration [28]. However, the effectiveness of a single therapeutic modality is limited, and the complexity of the preparation process is a factor to be considered. Therefore, modulation of wound glucose levels and remodeling of the microenvironment of diabetic wounds are beneficial for wound healing in diabetic patients.

Among the many modalities of glucose regulation, the classical glucose oxidase (GOx) catalyzes the in situ reduction of glucose concentration [4,29] and is uniquely suited to improve the high glucose microenvironment of wound surfaces. It has been demonstrated that physisorbed GOx can effectively catalyze the conversion of glucose to glucuronic acid and hydrogen peroxide (H_2O_2) [30], a process that regulates local pH to a slightly acidic level, which is consistent with normal

* Corresponding author.
** Corresponding author.
E-mail addresses: yangzhangyou@cqmu.edu.cn (Z. Yang), yuchao@cqmu.edu.cn (C. Yu).
[1] X.Y. and X.F. contributed equally to this work.

https://doi.org/10.1016/j.mtbio.2022.100308
Received 28 March 2022; Received in revised form 24 May 2022; Accepted 26 May 2022
Available online 2 June 2022

wound pH and facilitates healing [29]. In addition, the H_2O_2 byproducts produced can be used for antimicrobial purposes [30]. Nevertheless, the accumulation of H_2O_2 caused by rapid glucose removal can disrupt the redox homeostasis of the wound microenvironment, further generating excess ROS (e.g., superoxide anion [31], hydroxyl radical [32]) and causing toxic side effects, which is the main reason limiting the application of GOx. Under normal redox homeostasis, the cellular antioxidant system can effectively scavenge excess ROS, such as catalase (CAT), to remove H_2O_2 and superoxide dismutase (SOD) to remove superoxide anions [33]. However, when redox homeostasis is imbalanced, excess ROS can lead to oxidative stress [34], which irreversibly damages proteins, lipids and DNA [35], and these substances are fundamental to diabetic wound healing. Therefore, if the byproducts of GOx can be well handled, it will help to break the bottleneck of this natural glucose "killer" application.

In recent years, nanotechnology has been increasingly applied to the biomedical field [36], especially nanomaterials for ROS scavenging [37]. Among them, ceria nanoparticles are rich in enzymatic activity and capable of scavenging a wide range of ROS that have been widely explored [38]. The surface Ce^{3+}/Ce^{4+} coexistence of ceria nanoparticles, mainly produced in the tetravalent state, is mainly produced responsible for scavenging H_2O_2 and hydroxyl radicals, and the trivalent state scavenges superoxide radicals [39]. The dynamic balance maintained by the two valence states endows ceria nanoparticles with a continuous variety of mimetic enzymatic activities, including SOD enzymes and catalase (CAT) [39]. It is noteworthy that the CAT activity of the ceria nanoparticles can remove the secondary product H_2O_2 of GOx and generate a cascade effect to further catalyze its generation of oxygen, improving hypoxia while solving the side effects caused by H_2O_2 accumulation. Meanwhile, ceria nanoparticles have been shown to promote cell migration and angiogenesis [40–42], which undoubtedly facilitates wound repair. Therefore, ceria nanoparticles have good potential to achieve pro-diabetic wound healing in combination with GOx.

While ceria nanoparticles offer clear potential benefits as an adjuvant to wound repair treatments, there are still multiple issues to resolve in the development of this strategy. One issue is that the drug-carrying ability of ceria nanoparticles is poor [43]. The emergence of metal-organic frameworks (MOF) structures has provided new ideas to solve the drug delivery problem, and they have the advantages of a large specific surface area, drug delivery and acid responsive disintegration [44,45]. For example, Sun et al. synthesized Ce-MOF-808 as precursors for combustion catalysts of volatile organic compounds [46]. Other studies have shown that the imidazole group has a coordinate bond with cerium ions, which can form a new Ce-MOF [47]. Unfortunately, most of the Ce-MOF materials have significantly increased particle size and are unstable, resulting in a striking loss of their enzymatic activity. Therefore, it is particularly important to develop stable nanoscale Ce-MOF-like structures to maintain their enzymatic activities [48]. In our previous work, we demonstrated the anchoring effect of phosphonic acid groups on cerium ions, which helps to enhance the stability of ceria nanoparticles [49]. Therefore, based on the ligand bonding interaction of bisphosphonic acid and imidazole groups with cerium ions, developing coassembly techniques to construct novel ceria nanoparticles with good loading delivery GOx function and rich enzymatic activity is a promising strategy to improve the microenvironment of diabetic wounds and promote wound healing.

According to these considerations, in this work, a Ce-derived multifunctional nanozyme system was developed based on coassembly technology for application to diabetic wound treatments. As shown in Scheme 1, alendronic acid (AL) and 2-methylimidazole (HMIM) formed dual-ligand molecules that were subjected to Ce-driven coassembly to form nanoparticles CHA and embedded GOx to form the nanozymes (CHA@GOx) with multiple enzyme activities. It was verified that this system would mimic SOD and CAT activities and would achieve synergistic repair of diabetic wounds with GOx. *In vitro* and *in vivo* experiments showed that CHA@GOx not only removed excess glucose and ROS and

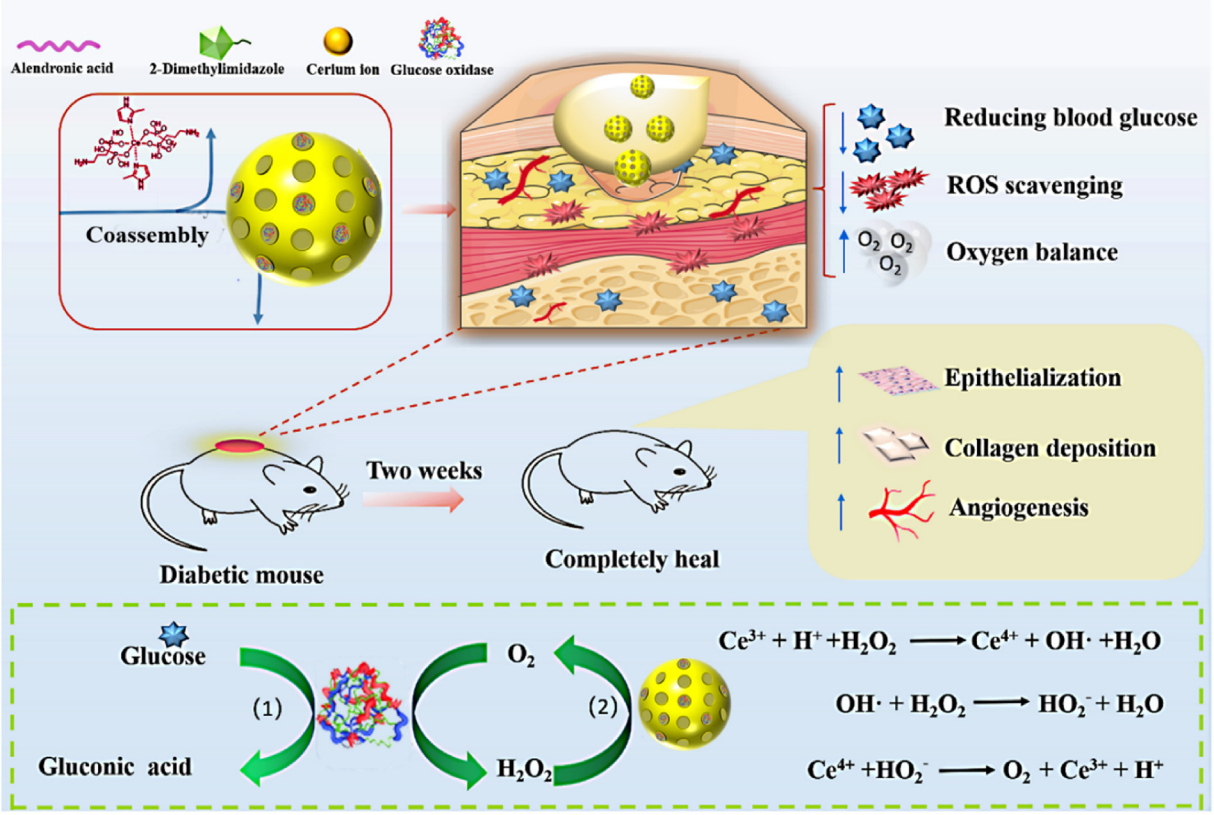

Scheme 1. Schematic diagram of Ce-driven coassembly multi-enzymatic activity of nanozyme for diabetic wound healing.

regulated oxygen balance but also supported cell migration and promoted the formation of cell tubes. Finally, CHA@GOx promoted angiogenesis, collagen deposition, and re-epithelialization during wound healing in diabetic mice, and it exhibited good biocompatibility. These results suggest that this novel multifunctional nanozyme will be useful in the treatment of diabetic wounds.

2. Materials and methods

2.1. Materials

Cerium (III) nitrate hexahydrate (Ce $(NO_3)_3{\cdot}6H_2O$), glucose (Glu), curcumin, alendronate (AL), Tris (2,2-bipyridine) ruthenium chloride (Ru(ddp)), 2-methylimidazole (HMIM), IR780, IR783, IR808, Ce6, Cy3, copper nitrate trihydrate ($Cu(NO_3)_2{\cdot}3H2O$), manganese dichloride ($MnCl_2$), magnesium chloride ($MgCl_2$), cobalt chloride ($CoCl_2$), iron trichloride ($FeCl_3$) and streptozotocin (STZ) were provided by Sigma–Aldrich (USA). Chlorin e6 (Ce6) was obtained from Frontier (UK). Glucose oxidase (GOx) and nitrotetrazolium blue chloride (NBT) were purchased from TCI (Japan). Methyl red, 2′,7′-dichlorofluorescin diacetate (DCFH-DA), hematoxylin-eosin (H&E), Masson's trichrome, Sirius staining solution and dihydroethidium (DHE) were purchased from Beyotime Biotechnology (China). Penicillin–streptomycin solution (100X), fetal bovine serum (FBS), trypsin and Dulbecco's modified Eagle's medium (DMEM) and RPMI-1640 medium (1640) were obtained from Gibco (USA). The Cell Counting Kit-8(CCK-8 kit) was purchased from MCE (USA). Anti-CD31 antibody, anti-α-SMA antibody and goat anti-rabbit IgG secondary antibody were purchased from Abcam (UK). High-purity (Milli-Q) water with a resistivity of 18.2 MΩ cm was obtained from an inline Millipore RiOs/Origin water purification system.

2.2. Characterization

The size distribution of the prepared CHA@GOx was measured by atomic force microscopy (AFM SPM-9700, SHIMADZU, Japan), transmission electron microscopy (TEM) and Malvern particle size analysis (DLS Zetasizer Nano ZS ZEN3600, UK). Subsequently, UV–vis spectrophotometry (UV–vis Ultra-6600A, Rigol, China) and Fourier infrared spectroscopy (FT-IR Nicolet iS5, Thermo Fisher Scientific, USA) were used to measure the special peaks and infrared absorption profiles of GOx in the nanozymes. Inductively coupled plasma–mass spectrometry (ICP–MS, Agilent 7500ce, America) was used to measure the concentration of cerium ions in CHA@GOx. Furthermore, the proportion of the trivalent state and the tetravalent state of cerium ions were measured with X-ray photoelectron spectroscopy (XPS, Escalab Xi+, USA). Finally, the instruments used in any other part included a pH meter (METTLER TOLEDO, USA), ordinary microscope (OM, NLCD500, China), inverted fluorescence microscope (IFM Nikon Corporation, Japan), microplate reader (MIR Thermo Fisher Scientific, USA), portable dissolved oxygen tester (DOT Ray Magnetic JPBJ-608, China), flow cytometry (FCM, BD FACSCalibur, USA), and small animal imaging system (SAIS, BI2AHE006, Korea).

2.3. The optimized experiment of ligand concentration

In the exploratory phase, after mixing 1 mL each of AL (1, 5, 10, 15, 20 mg/mL) and HMIM (1, 5, 10, 15, 20 mg/mL) using the controlled variable method, 100 μL of $Ce(NO_3)_3{\cdot}6H_2O$ solution (0.1 M) was slowly added dropwise and stirred at room temperature for 2 h. After dialysis purification for 24 h, the products were collected, and the particle size of each reaction product was measured by DLS to determine the final reaction concentration.

2.4. Synthesis of CHA@GOx

CHA@GOx was prepared based on a previous procedure with some modifications. In short, 1 mL each of the AL (10 mg/mL) and HMIM (10 mg/mL) aqueous solutions was mixed thoroughly; then, 100 μL of 0.1 M $Ce(NO_3)_3{\cdot}6H_2O$ solution was slowly added, and the mixture was stirred for 10 min. Furthermore, 100 μL of GOx (1 mg/mL) was added, and the reaction was maintained for 2 h. Finally, the products were obtained by dialysis with ultra-pure water for 24 h. Additionally, CHA was synthesized without the addition of GOx.

2.5. Loading capacity of CHA

To study the loading capacity of CHA, 5 μL of different dyes (IR780, Ce6, IR783, Cy3, IR808, 10 mM) was added to the premixed CHA solution, and the reaction was continued for 2 h, followed by dialysis purification for 24 h. Finally, the products were collected, and the drug loading capacity was measured by photographing and UV–vis spectrophotometry.

2.6. The versatility of dual ligands

The universality of ligands was verified by different metal donors. In the case of constant ligand solution, 0.1 M Ce^{3+} were replaced with different metal ions (Co^{2+}, Fe^{3+}, Mn^{2+}, Cu^{2+}, Mg^{2+}, Ca^{2+}). Briefly, 1 mL of each of the AL (10 mg/mL) and HMIM (10 mg/mL) aqueous solutions was mixed thoroughly. Then, 100 μL of 0.1 M different metal ion solutions were slowly added. The mixture was stirred for 2 h, followed by dialysis purification for 24 h. Finally, the products were collected, and the formation of nanoparticles was measured by photography, DLS and AFM.

2.7. Encapsulation efficiency and activity measurement of GOx

To evaluate the encapsulation efficiency of GOx in CHA@GOx, a standard GOx concentration curve (0.02, 0.04, 0.06, 0.08, 0.1, 0.2 mg/mL) was established by measuring the absorbance of the ultraviolet wavelength at 280 nm. The pH value was characterized by a pH meter, and color changes after the addition of methyl red were used to verify the activity of GOx. Namely, 1 mg/mL or 4 mg/mL glucose was added to 1 mL of CHA@GOx (equivalent to Ce ions: 3.5 mM, GOx: 0.037 mg/mL) solution, and the different reaction times were carried out at 37 °C.

2.8. CAT and SOD enzyme activity test

The method of verifying mimic-CAT activity was to add 20 μL of H_2O_2 (1 M) to 1 mL of CHA or CHA@GOx aqueous solution (equivalent to Ce ions: 3.5 mM) and continuously monitor the changes in dissolved oxygen within 15 min. The SOD-like activity of the nanozymes was measured by the riboflavin-photoreduction nitro blue tetrazolium (NBT) method. First, 50 μL of working solution was added to every 100 μL of CHA or CHA@GOx of different concentrations (Ce ions at concentrations of 0.5, 1, 2, 4, 8, and 16 μM correspond to GOx concentrations of 0.034, 0.068, 0.137, 0.274, 0.548, and 1.096 μg/mL) under dark conditions in a 96-well plate. Then, after shaking, the plate was placed under an incandescent lamp for 10 min. Last, a microplate reader measured the absorbance at 560 nm wavelength.

Here, the working solution is a mixture of 800 μL ethylenediaminetetraacetic acid solution (0.1 M), 300 μL NBT solution (2 mM), 200 μL riboflavin solution (0.6 mM) and 11.4 mL phosphate solution under light-proof conditions.

2.9. Biocompatibility analysis in vitro

2.9.1. Cytotoxicity tests

Mouse fibroblasts (NIH-3T3, Qingqi Biotechnology, China) were maintained in DMEM supplemented with 10% fetal bovine serum (FBS: Corning) and 1% penicillin streptomycin. Human umbilical vein endothelial cells (HUVECs, ScienCell, USA) were maintained in RPMI-1640

supplemented with 10% FBS and 1% penicillin streptomycin. These cells were maintained at 37 °C with 5% CO_2 and 95% relative humidity.

The cytotoxicity of CHA@GOx was assessed by the CCK-8 cell viability kit assay. In short, NIH-3T3 or HUVECs were seeded in a 96-well plate and cultured for 24 h and then treated with different concentrations of CHA, CHA@GOx (0, 5, 10, 20, 40, 80, 160 μM, calculated based on cerium ions content) and GOx (equivalent to CHA@GOx) for 8 h. Subsequently, the cells were rinsed well with PBS, and CCK-8 solution was added to each well to a concentration of 10%. The plate was incubated at 37 °C, and the absorbance was measured at 450 nm.

2.9.2. Hemocompatibility assay

Mouse whole blood was used to prepare a 5% red blood cell suspension. The PBS group was used as a negative control, and the sodium dodecyl sulfate group was used as a positive control. Meanwhile, different concentrations of CHA or CHA@GOx (0, 5, 10, 20, 40, 80, 160 μM) were placed in an environment of 5% red blood cells and left for 6 h. After taking pictures and then centrifuging at 3000 rpm/min for 5 min, the upper suspension was aspirated, and the degree of erythrocyte rupture was measured at 541 nm. Finally, the hemolysis rate (HR) was calculated by Equation (1) below:

$$HR = (AS - AN) / (AP - AN)*100\% \quad (1)$$

Here, AS, AP, and AN represent the absorbance of samples, positive control, and negative control at 541 nm, respectively.

2.10. Intracellular ROS scavenging

To study the intracellular ROS scavenging ability of the nanozymes, HUVECs were seeded in 6-well plates ($6*10^4$) and incubated for 24 h. Then, after stimulation with H_2O_2 (100 μM) for 12 h, different sample groups (PBS, H_2O_2, CHA + H_2O_2, GOx, CHA@GOx and CHA@GOx + H_2O_2, 5 μM) were added and incubated for 8 h. Next, the cells were rinsed with PBS three times before adding the ROS-specific probe 2,7-dichlorodihydrofluorescein diacetate (DCFH-DA, 10 μM). Finally, the fluorescence in the HUVECs was observed by IFM.

2.11. Intracellular oxygen production

For intracellular oxygen studies, NIH-3T3 cells were cultured using DMEM under 1% oxygen and 37 °C conditions. After the formation of a monolayer of hypoxic cells, the cells were treated with H_2O_2 (20 μM) and different drugs (PBS, GOx, CHA, CHA@GOx, 5 μM) for 8 h. Then, the cells were incubated with Ru(ddp) (2 mM) for 2 h, rinsed with PBS 3 times and subjected to fluorescence imaging by IFM. The fluorescence intensities were quantified using ImageJ software (NIH, Bethesda, MD).

2.12. Phenotype of macrophages

Macrophage typing assays were used to assess the effect of CHA@GOx on immune cells. Primary macrophages were seeded in 24-well plates ($2*10^5$ cells/well) in DMEM supplemented with 10% FBS and 1% penicillin streptomycin. Macrophage typing was then observed by FCM under different treatment conditions. (1) Macrophages were treated with PBS, GOx, HCA or CHA@GOx (5 μM) for 8 h and then fluorophore-labeled antibodies (F4/80, CD80, CD206: 0.5 μL each/test, BioLegend, USA) were used to detect F4/80, CD80 and CD206 antigen expression in each group of cells. (2) Macrophages were first treated with LPS and TNF-α for 12 h, and then the steps of experiment (1) above were repeated.

2.13. Cell scratch test

To perform the cell migration assay using high glucose medium (DMEM: 6000 mg/L glucose), NIH-3T3 cells were first cultured in a six-well plate ($8*10^4$ cells/well) to reach 85–95% cell density. Then, the monolayer was scraped with a 10 μL pipette tip. After removing the cell debris, serum-free medium containing PBS, CHA or CHA@GOx (5 μM) was added for treatment, and images were collected and the migration rate was calculated within the required time interval (0, 12, 24 h). The migration rate (MR) was calculated by Equation (2) below:

$$MR = (A_0 - A_T) / A_0*100\% \quad (2)$$

Here, A_0 and A_T refer to the area of the scratch at 0 h and T h, respectively.

2.14. Tube formation experiment

To observe tubule formation, HUVECs were pretreated with different drugs (PBS, GOx, CHA, CHA@GOx, 5 μM) and high glucose medium (1640:3000 mg/L glucose) for 8 h. Then, matrigel (model 356234, Corning, USA) was added to a 48-well plate (50 μL per well), and the plate was placed in a 37 °C incubator for 40 min for solidification. Meanwhile, the previously processed cells were digested, and 100 μL cells were added to matrigel at approximately $2*10^4$ cells per well and incubated for 12 h. The photos were taken, and ImageJ software was used to simulate the length of the tubules and the number of tubule connections.

2.15. Biodegradability and biocompatibility of CHA@GOx in vivo

Using *in vivo* imaging to observe the degradation of nanozymes, near-infrared fluorescent dyes (IR783) marked CHA and CHA@GOx were first synthesized. BALB/c mice were subcutaneously injected with free IR783, 783-CHA or 783-CHA@GOx (50 μL, equivalent to Ce ions: 20 μM). The imaging was performed at different time points after injection with a small animal imaging system. To further examine the biocompatibility of nanozymes in mice, three days after the injection of PBS or CHA@GOx subcutaneously into the backs of mice, blood samples were collected for routine blood examination and centrifuged to collect serum for biochemical testing. Then, the skin of the injection site and main organs were stained with H&E.

2.16. Wound treatment of normal mice

The *in vivo* wound healing induced by the nanozymes was performed by a splinted excisional wound model in healthy male C57BL/6 mice. For surgical excisional wounds, the dorsal hairs of the mice were first shaved. A full-thickness skin wound of approximately 1 cm^2 was made on the back of each mouse. Then, the wounds were randomly allotted into four groups (n = 3): PBS, GOx, CHA and CHA@GOx groups. In the first three days of wound establishment, 25 μL of different samples (equivalent to Ce ions: 10 μM) were applied to the skin once a day, and every three days, the wounds were observed.

2.17. Wound treatment of diabetic mice

To establish a mouse model of diabetes, all animal experiments were performed strictly in accordance with the regulations of Chongqing Medical University (SCXK2018-0003). Approximately 20 g of male BALB/c mice were obtained from the Experimental Animal Center of Chongqing Medical University and reared under standard conditions. After one week of normal feed, they received high-fat feed (MD12033) and continued to feed for two weeks. After fasting for 12 h before administration, 1% streptozotocin (STZ) was injected intraperitoneally to induce the mice to establish the hyperglycemic model at a dose of 50 mg/kg. After the injection, they continued to fast for 2 h, and STZ was injected once a day for 5 consecutive days. Blood glucose was measured one week later, and the tail vein blood glucose was more than 16.7 mmol/L, which was regarded as a successful induction of the hyperglycemia model. Finally, the mice were anesthetized by the intraperitoneal

injection of sodium pentobarbital (0.3%, per 100 g), and a biopsy punch with a diameter of 1 cm was used to take the full-thickness skin of the back of the mouse and fix the wound with tissue glue and a rubber ring (Φ1.5 × 1.3).

Next, the above mice were randomly divided into 4 groups (PBS, GOx, CHA and CHA@GOx, n = 7), and in the first three days of wound establishment, 25 μL of different samples (equivalent to Ce ions: 10 μM) was applied to the skin. Meanwhile, the wound condition, weight and blood glucose data were collected every 3 days for two weeks.

2.18. Histological and immunofluorescence analysis

At different times (3, 7, and 14 days), the wound tissue was taken and fixed with 4% paraformaldehyde, paraffin-embedded, sliced into approximately 5 μm sections, and finally stained with H&E, Masson's trichrome and Picrosirius red to evaluate wound healing. For immunofluorescence evaluation, the deparaffinized and rehydrated sections of the treated wound tissue (7, 14 days) were combined with anti-CD31 antibody (ab199012, 1:200) and anti-α smooth muscle actin antibody (ab7817, 1:200) and incubated overnight at 4 °C. Then, the corresponding fluorescently labeled secondary antibodies (Alexa Fluor/ab150077 and ab150115, 1:400) were used. Similarly, the wound tissue (14 days) was frozen and sectioned and incubated with ethidium dihydrogen (DHE, 2 μM) at 37 °C for 30 min to measure the overall superoxide content of the sample. The nucleus was stained with hematoxylin or DAPI dihydrochloride (C1006, Beyotime). Finally, the tissue sections and immunofluorescence sections were observed with an ordinary microscope (NL CD500, China) and an inverted fluorescence microscope (IFM Nikon Corporation, Japan), respectively.

2.19. Statistical analysis

All quantitative results are expressed as the mean ± sd. Statistical analysis was performed by using two-tailed unpaired Student's t tests. The data are indicated with * when $p < 0.05$, ** when $p < 0.01$, and *** when $p < 0.001$. Statistical evaluations of experimental data were conducted using GraphPad Prism 6.0 software.

3. Results and discussion

3.1. Preparation and characterization of CHA and CHA@GOx

CHA@GOx was prepared by coassembling GOx with dual-ligand molecules (AL and HMIM) and cerium ions, as shown in Fig. 1A. CHA was first prepared without GOx. Prior to that, we investigated the influence of the molar ratio of AL and HMIM on nanoparticle characteristics by synthesizing a series of CHA nanoparticles using the controlled variable method. Dynamic light scattering (DLS) was used to detect the hydrated particle size of CHA. As shown in Fig. S1, when the molar ratio of AL and HMIM to cerium ions was 1:1:0.43, uniformly dispersed CHA with a size of approximately 10 nm was obtained. Based on the structural characteristics of the ligand molecule, we believe that the cerium ions and the dual-ligand molecules are combined through ordered coordination (Fig. S2). In addition, further DLS analyses (Fig. S3) showed that the size of the nanoparticles increased to 35 nm after coassembly with GOx to form CHA@GOx.

Next, we further investigated the structure of the prepared CHA and CHA@GOx. By analyzing the TEM and AFM images of CHA and CHA@GOx (Fig. 1B–E), we found that CHA and CHA@GOx both formed uniformly dispersed spherical nanoparticles. CHA forms particles with diameters of approximately 8 nm, and CHA@GOx forms particles with sizes of approximately 20 nm. These sizes are conducive to the presentation of simulated enzyme activity [50,51]. Additionally, UV–vis examination demonstrated that free GOx and CHA@GOx that had been disintegrated under acidic conditions had the same UV–vis absorption peak at 280 nm (Fig. 1F). Incorporation of GOx into CHA@GOx was further demonstrated by comparison of the FT-IR spectra of free GOx and CHA@GOx (Fig. 1G). Both samples presented confirmatory FT-IR peaks at 1646 cm^{-1}, 1526 cm^{-1} and 1240 cm^{-1}. Overall, these results demonstrate the successful synthesis of CHA@GOx.

The delivery capability of nanoparticles is beneficial to broadening the applications of nanomaterials [52,53]. Therefore, we investigated the potential of CHA for drug delivery. Both the images and UV–vis absorption spectra shown in Fig. 1H and Fig. S4 demonstrated that cerium ions could drive the coassembly of different dye molecules to form nanoparticles. Meanwhile, the results of nitrogen adsorption also showed that CHA has a specific surface area of 1.5447 m^2/g and a pore size of approximately 2 nm (Fig. S5A-B), providing further evidence for the possible enzymatic activity and drug-carrying capacity of CHA, thus expanding its potential for therapeutic applications in other diseases. Furthermore, to investigate the versatility of the proposed bisphosphonic acid-imidazole double ligand system, other metal ions (including Fe^{3+}, Mg^{2+}, Mn^{2+}, Cu^{2+}, Co^{2+} and Ca^{2+}) were tested for their ability to replace cerium ions. The DLS and AFM results (Fig. S6A-B) showed that in addition to cerium ions, there were a variety of metal ions that could participate in the bisphosphonic acid-imidazole coassembly system to form nanoscale particles, demonstrating the universality and potential application of this system.

3.2. Enzymatic activity of CHA and CHA@GOx

The dynamic balance of Ce^{3+} and Ce^{4+} is crucial for the simulated CAT and SOD activities of ceria-related nanomaterials. X-ray photoelectron spectroscopy (XPS) was used to analyze the valence distribution on the surface of CHA@GOx. As shown in Fig. 2A, the surface cerium ions consist of approximately 57.5% and 42.5% Ce^{3+} and Ce^{4+}, respectively. Here, the original concentration of cerium ions in the solution was measured by ICP–MS to be 3.5 mM (Fig. S7), and the above results suggested that CHA@GOx is promising for applications in the field of enzyme-mimicking catalysis [54]. Therefore, we next explored the SOD-like enzyme activity of these nanozymes. As seen from Fig. 2B, both CHA and CHA@GOx had strong SOD-like activities, as demonstrated by the 72.5% and 65.9% inhibition of free radicals when the concentration of cerium ions was 16 μM, respectively. In addition, since CAT catalyzes the production of oxygen from H_2O_2, the CAT activities of CHA and CHA@GOx were investigated by monitoring the oxygen content of the solution. We found that the concentration of dissolved oxygen in the CHA and CHA@GOx systems increased by 40% and 32%, respectively, 15 min after the addition of H_2O_2 to the solution (Fig. 2C). Meanwhile, the colors of both solutions changed from colorless to yellow with obvious bubble production (Fig. 2D). This color change represents H_2O_2-mediated induction of the transition of surface ions from the Ce^{3+} to the Ce^{4+} oxidation state [55], as the CAT-mimic enzyme activity catalyzes the production of oxygen from H_2O_2.

To further study the loading dose of GOx in CHA@GOx, we constructed a standard curve of GOx (Fig. S8) and obtained a loading rate of 37% GOx in CHA@GOx. Subsequently, to investigate whether the GOx activity was well maintained after coassembly, the activity of CHA@GOx was evaluated in response to the addition of glucose. It is well known that the process of glucose catalysis by GOx is accompanied by glucuronide production, so the change in pH can indicate the catalytic activity of GOx. As shown in Fig. 2E, reactions in which glucose was added to a suspension containing CHA nanoparticles and a pH indicator showed a UV–vis spectrum characteristic of basic methyl red (λ_{max} = 435 nm), and the solution was yellow, indicating a pH between 4.4 and 6.2. However, after the reaction of free GOx with glucose, the pH decreased, as indicated by a color change to pink (pH ≤ 4.4) and a UV–vis spectrum characteristic of acidic methyl red (λ_{max} = 530 nm). Similarly, after CHA@GOx reacted

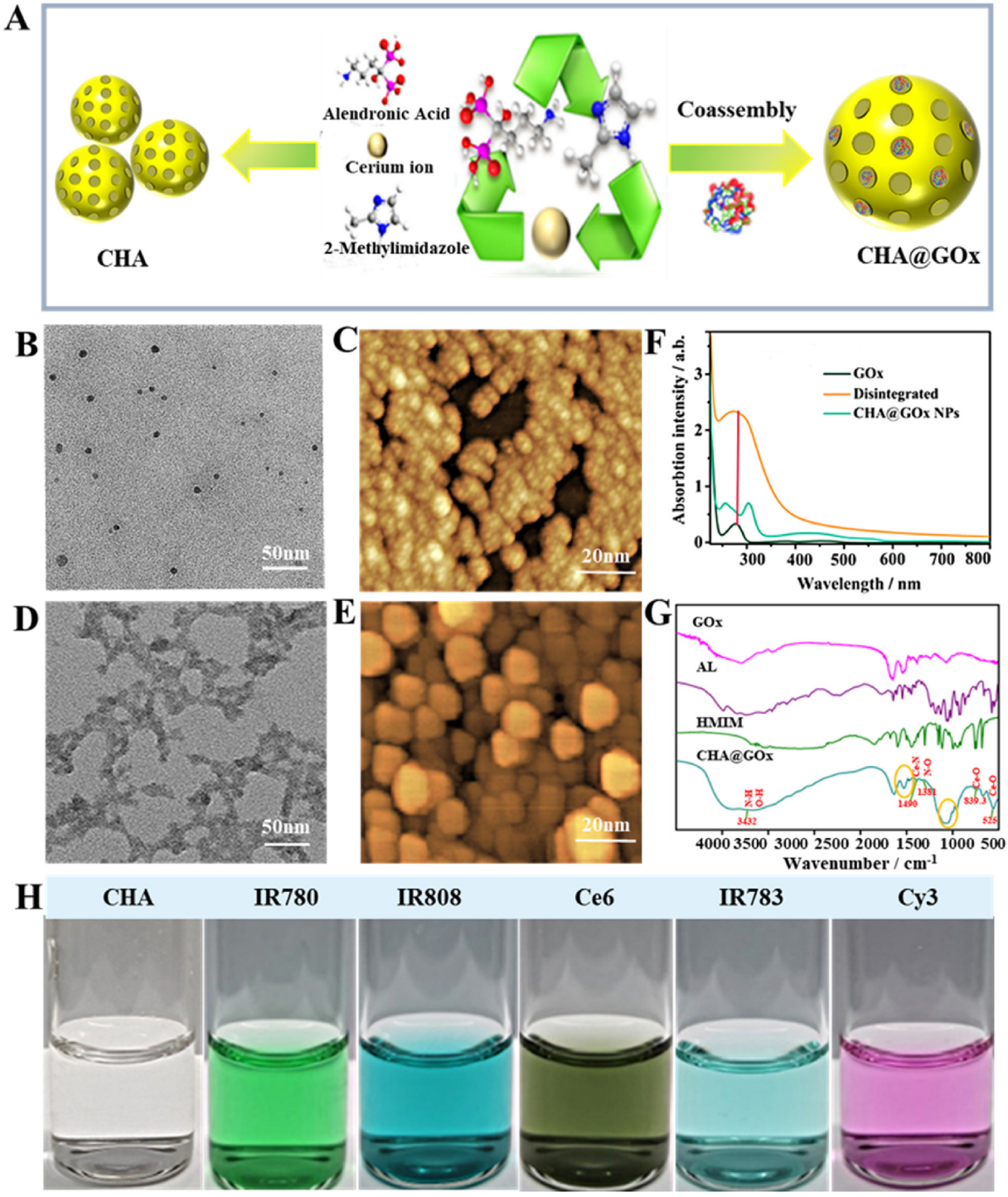

Fig. 1. Characterization of CHA@GOx. A) Scheme of preparing CHA and CHA@GOx. B) TEM image of CHA. C) AFM image of CHA. D) TEM image of CHA@GOx. E) AFM image of CHA@GOx. F) UV–visible absorption spectra of GOx in CHA@GOx at 280 nm. G) FT-IR spectra of CHA@GOx. H) Images of the co-assembly of CHA with different dyes.

with glucose, the solution became acidic, suggesting that the GOx after coassembly remained active, accompanied by the potential disintegration of the nanozymes under acidic conditions. On this basis, we further demonstrated the activity of GOx in CHA@GOx and the acidic disintegration of nanozymes induced by an *in vitro* glucose-responsive disintegration assay (Fig.S9). In particular, the CHA@GOx + Glu (4 mg/mL) group showed significant solution turbidity, and the measured AFM results showed no nanoparticle morphology at 24 h.

To investigate this phenomenon, a pH meter was used to quantitatively follow the pH changes. We added two concentrations of glucose (4 mg/mL and 1 mg/mL) to CHA@GOx to simulate the high and normal glucose concentrations within wounds. As shown in Fig. 2F, CHA@GOx was able to catalyze glucose, leading to a gradual decrease in pH over 24 h. This resulting pH range has been proven to be beneficial to chronic wound healing [56].

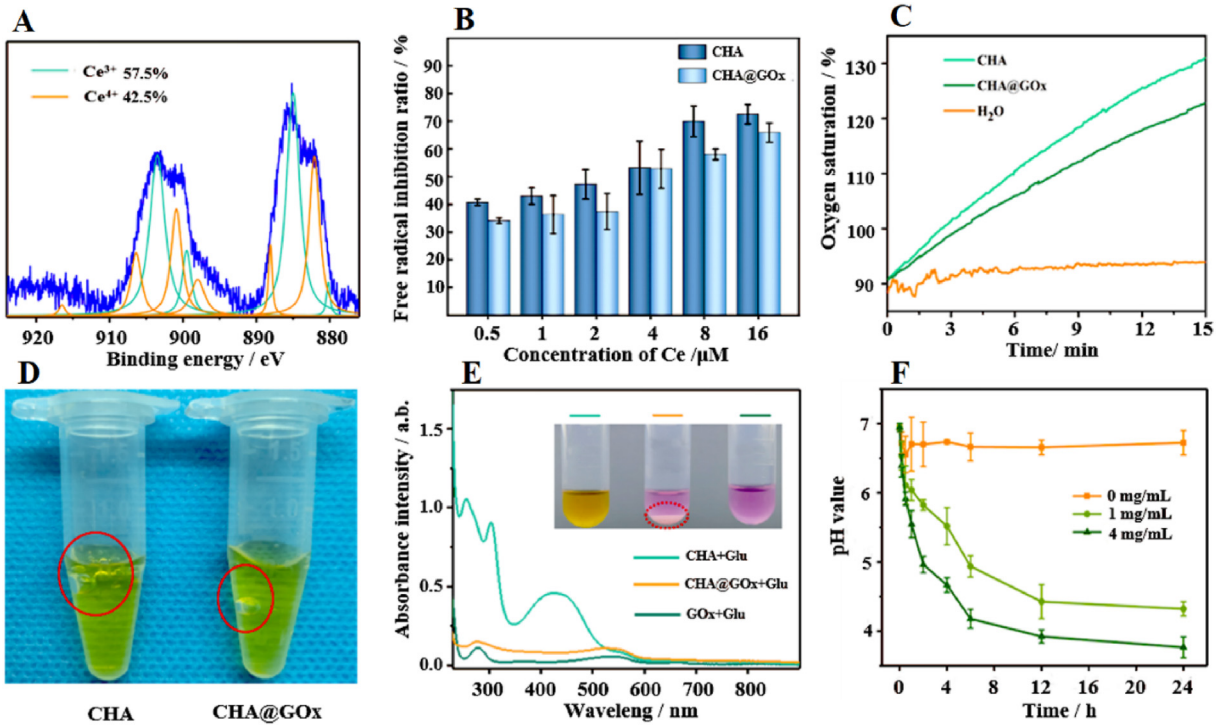

Fig. 2. Enzymatic activity verification of CHA and CHA@GOx. A) The concentration detected of Ce^{3+} and Ce^{4+} in CHA@GOx by XPS. B) The activity of mimic-SOD. C) The activity of mimic-CAT. D) Picture of CAT simulating enzymatic activity catalyzing oxygen production from H_2O_2. E) The activity of GOx in CHA@GOx by UV–vis and methyl red (grouped into CHA + Glu, CHA@GOx + Glu, GOx + Glu, respectively). F) pH changes within 24 h (glucose content: 0 mg, 1 mg, 4 mg).

3.3. Cytotoxicity, ROS scavenging and the ability to regulate the oxygen balance of CHA@GOx

The safety of nanozymes is important for their application *in vivo*. Therefore, we used a hemolysis activity assay to observe the effects of different concentrations of CHA@GOx on red blood cells. These red blood cells remained nonhemolytic even at high doses of CHA@GOx and were almost indistinguishable from those of the negative control group (Fig.S10). These results indicated satisfactory hemocompatibility for further biological applications. Then, cytotoxicity tests of CHA@GOx based on HUVECs cells or NIH-3T3 cells were performed, because endothelial cells and fibroblasts play important roles in wound healing [57–59]. CCK-8 analysis (Fig. 3A - B) showed that neither CHA nor CHA@GOx was significantly toxic to these two kinds of cells. Importantly, high concentrations of free GOx were found to be toxic to HUVECs and NIH-3T3 cells compared to similar concentrations of CHA@GOx. This toxicity is likely due to the rapid catalysis of glucose oxidation by GOx and the subsequent production of cytotoxic H_2O_2. In the CHA@GOx treatment groups, however, the CAT-simulating enzymatic activity of CHA effectively removed the H_2O_2 produced by the GOx reaction, thus reducing the toxic side effects of GOx.

To further verify the above ideas, we explored the ability of CHA to protect cells from ROS. To that end, H_2O_2 was added as a source of ROS, and 2′,7′-dichlorodihydrofluorescein diacetate was used as a fluorescent probe to indicate intracellular ROS. As shown in Fig. 3C–D and Fig.S11 A, after H_2O_2 treatment, the intracellular ROS increased significantly. By comparing cells treated with PBS, H_2O_2 or CHA and H_2O_2, it was found that CHA could effectively reduce the level of intracellular ROS. In addition, as described earlier, GOx catalyzes the oxidation of glucose to produce H_2O_2, so when cells were treated with free GOx without additional H_2O_2, significant fluorescence was detected. However, treatment of the cells with CHA@GOx significantly reduced the intracellular fluorescence. It is suggested that CHA@GOx can not only remove the ROS produced by GOx but also remove excessive H_2O_2, thereby reducing oxidative stress via its CAT-mimicking activity.

Previous studies have shown that cells exposed to a hypoxic microenvironment exhibit impaired angiogenesis and tissue regeneration. Therefore, we explored whether CHA@GOx could regulate the oxygen content in cells and rescue cellular activity even when tissues are under hypoxic conditions. We treated HUVECs with different preparations in a low oxygen (1% O_2) environment. Tris(2,2-bipyridine) ruthenium chloride hexahydrate was used as an oxygen-sensitive probe whose fluorescence was specifically quenched by the oxygen molecule [60], so that the fluorescence intensity was inversely proportional to the oxygen content. As seen in Fig. 3E–F and Fig.S11B, the intracellular fluorescence in the presence of the GOx group was the most obvious, suggesting that GOx consumes part of the oxygen. However, the fluorescence intensity of cells in the presence of CHA and CHA@GOx was significantly reduced compared to cells treated with PBS and GOx, which was due to the CAT-mimicking enzyme activity of CHA and CHA@GOx. Thus, these nanozymes were able to achieve an appropriate oxygen balance and prevent further cellular damage.

3.4. Evaluation of the impact of CHA@GOx on macrophage phenotype, cell migration and cell tube formation in vitro

Diabetic wounds are also characterized by a prolonged inflammatory phase and an abnormal macrophage phenotype. In the above experiments, we demonstrated that CHA@GOx can scavenge excess ROS and regulate oxygen homeostasis. Therefore, we next assessed the effect of CHA@GOx on macrophages by flow cytometry, particularly M1 macrophages. As shown in Fig.S12A, the CHA@GOx group promoted both M1 (CD80) and M2 (CD206) polarization of macrophages compared to any other group, but more so the M2 polarization. Subsequently, after LPS and IFN-γ stimulated macrophages differentiation to the M1 type, we treated the cells with different drugs and found that the CHA@GOx group was able to significantly reduce macrophages CD80 expression but increase CD206 expression compared to the other groups (Fig.S12B). The above experiments suggest that CHA@GOx may help to resolve inflammation and promote the repair process to the next stage.

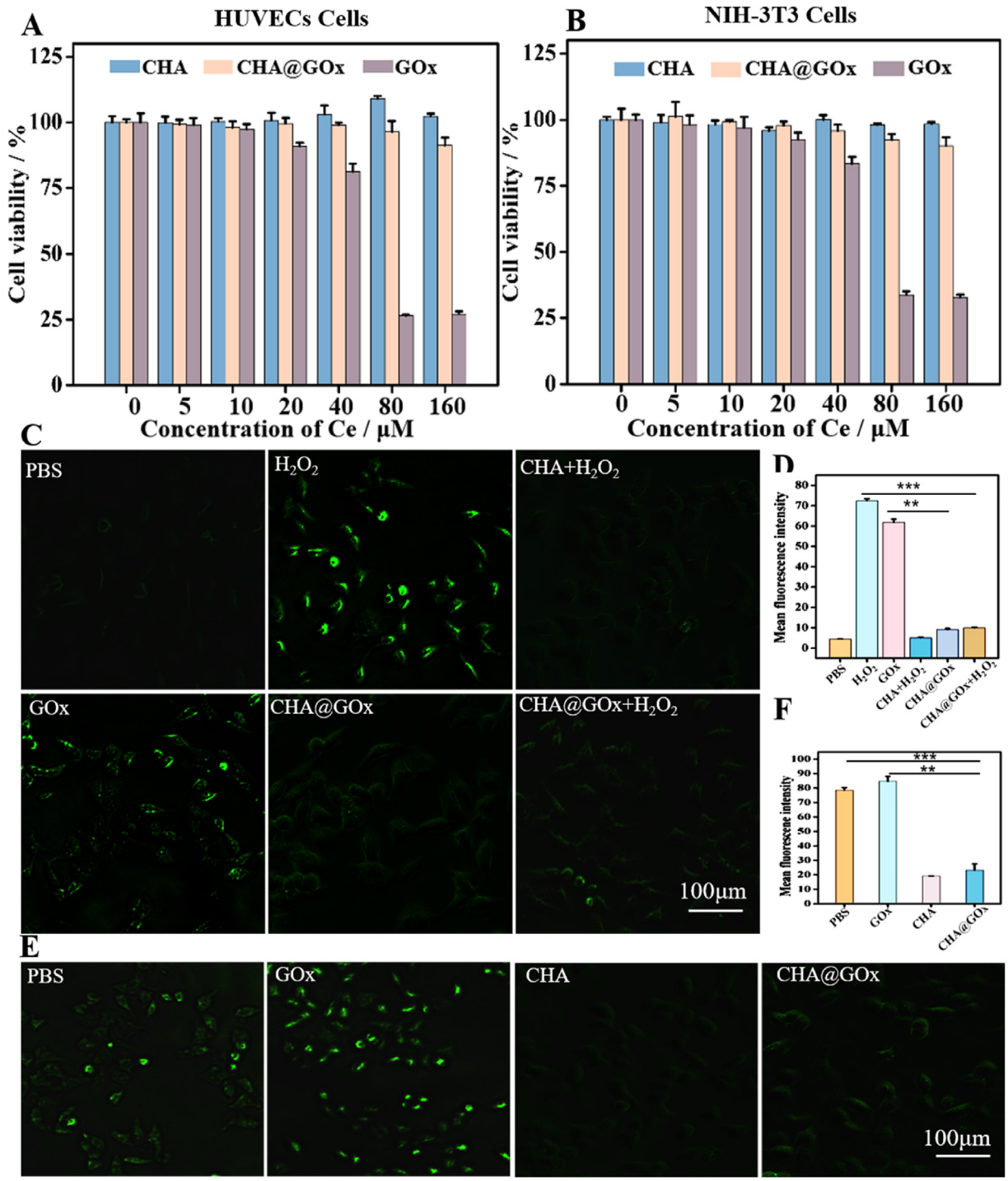

Fig. 3. Cytotoxicity, ROS scavenging and ability to regulate oxygen balance of CHA@GOx *in vitro.* A)Cell viability of HUVECs cells after incubation with different samples (CHA, CHA@GOx, GOx). B)Cell viability of NIH-3T3 cells after incubation with different samples (CHA, CHA@GOx, GOx). C) DCFH-DA assay detecting intracellular ROS level of HUVECs cells after different treatments. D) Fluorescence of intracellular ROS level is quantified by ImageJ software. E) Ru(ddp) assay detecting intracellular O_2 level of HUVECs cells after different treatments. F) Fluorescence of intracellular oxygen is quantified by ImageJ software.

Given the role of fibroblasts in wound healing, promoting their migration can accelerate the healing of damaged skin, but a high glucose environment has been shown to inhibit this process [61]. To determine whether CHA@GOx can promote the migration of fibroblasts, we performed a scratch test. After incubating NIH-3T3 cells under various conditions for 24 h, the migration of cells treated with CHA or CHA@GOx was found to be more rapid than that of the control group. This effect was especially strong in the CHA@GOx-treated group (Fig. 4A - B). These results suggest that ceria nanozymes promote cells migration, and the reduction in the concentration of glucose in the environment by GOx further supported this migration-promoting effect. Meanwhile, the nanozymes can promote NIH-3T3 cells migration in a high glucose environment and thus provide conditions to promote wound healing.

In addition to fibroblasts, vascular cells are another important component of skin tissue, as they provide a pathway to deliver oxygen and nutrients to support wound healing [62]. Therefore, we investigated the effect of nanozymes on the production of vascular cells through the process of angiogenesis. HUVECs pretreated with different conditions

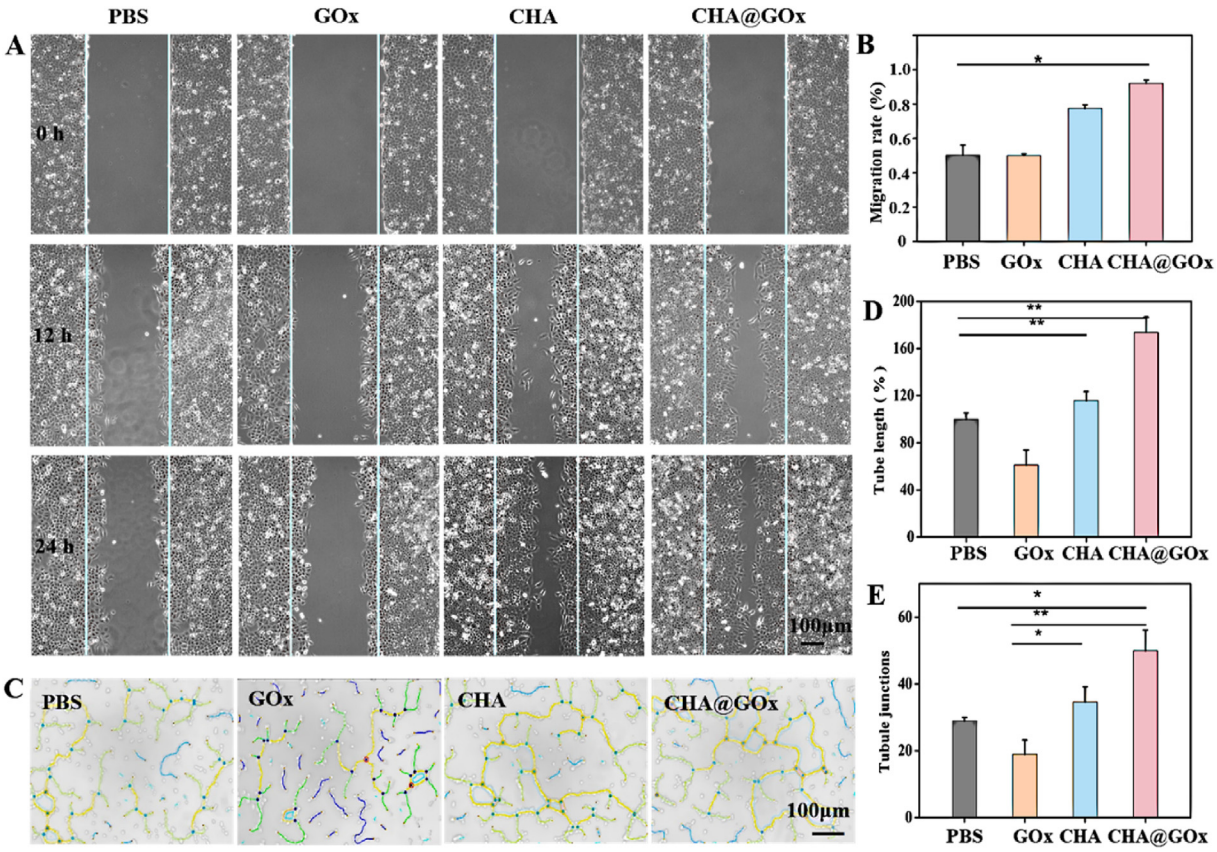

Fig. 4. The ability of CHA@GOx to promote cell migration and cell tube formation. A) Scratch test to analyze the migration ability of NIH- 3T3 cells at 0, 12, 24 h. B) Quantify NIH-3T3 cells migration rate. C) Tube experiment verifies the formation of tubes of HUVECs cells after different samples (PBS、GOx、CHA、CHA@GOx) are processed. D) The tube length and E)The tubule junctions are both measured by ImageJ software.

were transferred to matrigel and incubated for 12 h. As shown in Fig. 4C and D, the lengths of the cell tubes were obviously increased by treatment with CHA and CHA@GOx, and tubule junctions increased by approximately 5% with CHA treatment and 20% with CHA@GOx compared to treatment with PBS (Fig. 4E). However, cells treated with GOx performed poorly in angiogenesis assays. Here, the cells may have been negatively affected by high glucose in the early stages of growth, and then they were damaged by ROS produced by GOx. The enhanced angiogenesis upon treatment with the nanoparticles confirms the clear ability of ceria nanozymes to promote angiogenesis, and the regulated oxygen content also provides positive feedback. Thus, these results provide an additional basis for the application of these nanozymes for the acceleration of diabetic wound repair *in vivo*.

3.5. *In vivo degradation and safety study*

Studying the metabolism of drugs in the body helps to determine the time scale over which they are potentially active. In addition, the accumulation of drugs over a long time period may lead to more serious side effects. To evaluate the metabolism of nanozymes *in vivo*, CHA and CHA@GOx were labeled with IR783, which were called IR783-CHA and IR783-CHA@GOx. Subsequently, they were injected subcutaneously into mice, and the resulting images generated by a small animal imaging system are shown in Fig. 5A. Interestingly, the fluorescence of free IR783 rapidly subsided after subcutaneous injection and essentially disappeared by 12 h postinjection. In contrast, the fluorescence of IR783-CHA decreased slowly, and detectable fluorescence was observed even at 3 d postinjection. However, in animals injected with IR783-CHA@GOx, the fluorescence disappeared relatively rapidly. The rate of disappearance was not as rapid as that of free IR783, but it was faster than that in animals injected with IR783-CHA. This result is consistent with a model in which GOx released from CHA@GOx was controlled by blood glucose levels [36], and GOx-mediated degradation of glucose to glucuronic acid resulted in a local decrease in pH that gradually disrupted the structure of the nanozymes. Therefore, this disruption would result in an acceleration of the release and degradation of IR783-CHA@GOx. At the same time, the faster drug release of nanomaterial *in vivo* would be conducive to its application on the wound, and it would not be as likely to cause toxic side effects due to long-term accumulation.

To investigate the biocompatibility of the material, we injected identical volumes of PBS and CHA@GOx subcutaneously into the backs of mice. Three days later, blood and biochemical indicators were measured, and samples of skin from the injection site and of various organs were stained with H&E for histological evaluation. As shown in Fig. 5B and C, the blood and biochemical indicators of all mice were within normal ranges. Similarly, no obvious inflammation or damage was observed upon histological evaluations of skin and various organs of the CHA@GOx group or the PBS group, as shown in Fig. 5D. The above results suggest that CHA@GOx has good biosafety *in vivo*.

3.6. *In vivo evaluation of the acceleration of wound healing*

Encouraged by the impact of the nanozymes on cell migration and the promotion of tube formation *in vitro* and the *in vivo* safety profile, the effect of CHA@GOx in promoting wound healing was tested *in vivo*. First, we determined whether the nanozymes could promote the healing of normal wounds. Prewounded C57BL/6 mice were randomly divided into four groups to receive treatment with PBS, GOx, CHA or CHA@GOx. As shown in Fig. S13, when the wounds were analyzed after 14 days of treatment, it was found that mice treated with CHA and CHA@GOx

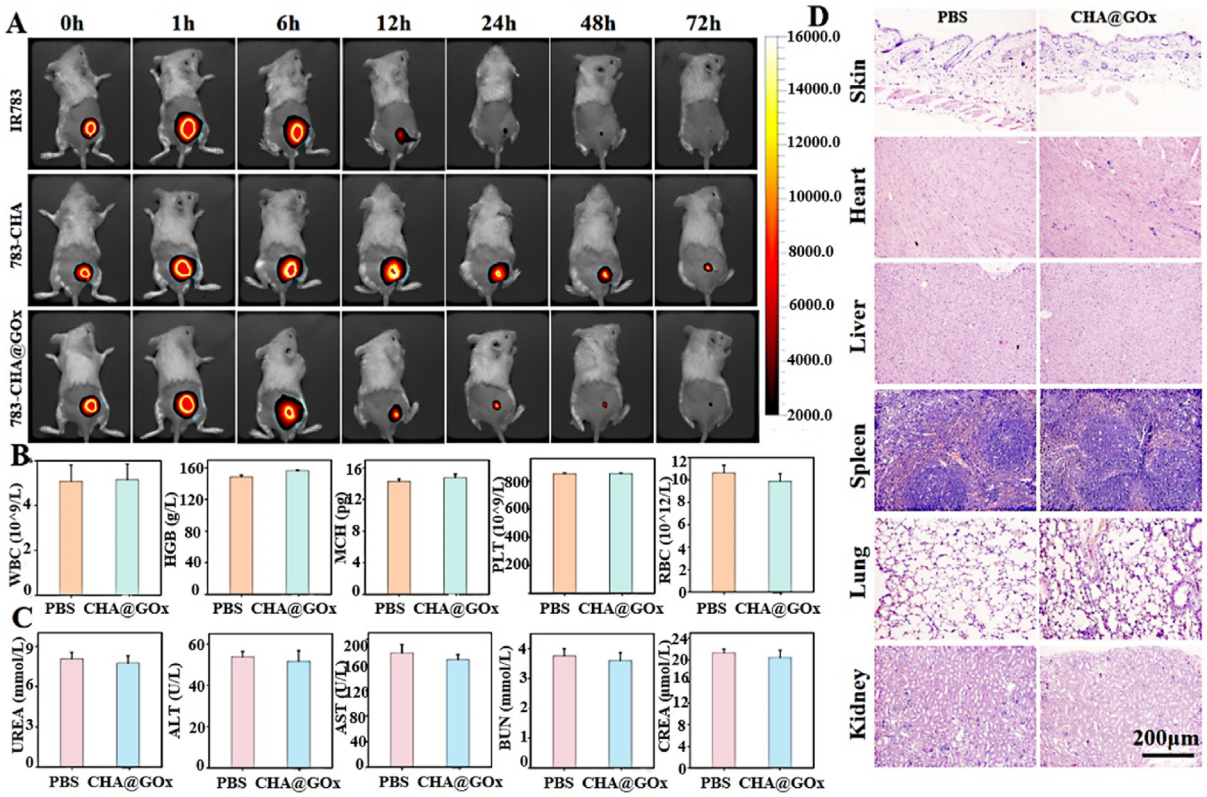

Fig. 5. *In vivo* fluorescence imaging and safety. A) Mice were imaged at the indicated time points after subcutaneous injection of IR783,783-CHA and 783-CHA@GOx. B) Results of routine blood analysis: white blood cells (WBC), hemoglobin (HGB), mean corpuscular hemoglobin (MCH), platelets (PLT) and red blood cells (RBC). C) Results of biochemical test: Serum urea (UREA), alanine aminotransferase (ALT), aspartate aminotransferase (AST), urea ammonia (BUN) and serum creatinine (CREA). D)H&E stained the sections of skin tissues and major organs at three days after subcutaneous injection of different drugs (GOx, CHA@GOx).

experienced better wound healing than did the PBS group. The main reason for this difference may be that the effect of ceria nanozymes in promoting cell migration and tube formation is helpful for wound healing. These results provided preliminary evidence that the nanozymes promote wound healing.

However, diabetic wounds are quite different from normal wounds due to their unique microenvironments. Therefore, mice were treated with streptozotocin to establish an animal model of diabetic wounds. As shown in Fig. 6A and Fig. S14, the blood glucose of the mice was consistently higher than 16.7 mmol/L, indicating that the diabetic mouse model was established successfully. Then, these prewounded mice were randomly divided into four groups and treated with PBS, GOx, CHA and CHA@GOx, as above, for a 14-day treatment period. To assess the wound healing process, the wounds were photographed every 3 days, and the wound area was calculated based on these images using ImageJ software. As shown in Fig. 6B and Fig. S15, we found that wounds healed slowly in mice treated with PBS and GOx; in contrast, mice treated with CHA@GOx experienced the most rapid wound healing. The results are consistent with a model in which the assembled GOx is slowly released under the control of the blood glucose concentration in the wound microenvironment in situ, thus decreasing the blood glucose level. On the other hand, the disintegrated ceria nanozymes not only remove excessive ROS and regulate oxygen balance but also accelerate cell migration and tube formation, which ultimately accelerates the healing of diabetic wounds.

Quantitative results showed that after two weeks of treatment, while the wound healing rates in mice treated with PBS or GOx were only 62% and 65%, respectively, the wound healing rate in mice treated with CHA was approximately 74%, and the healing rate increased to 88.5% in mice treated with CHA@GOx (Fig. 6C and Fig. S16). Importantly, the body weights of the mice did not change significantly (Fig. 6D), and blood glucose was maintained at high levels (Fig. 6E) during the treatment period. These results showed that CHA@GOx accelerates the healing of diabetic wounds through synergy without significant negative effects.

3.7. Histological and immunohistochemical analysis

To further evaluate wound healing in diabetic mice, histological analyses were performed. H&E staining was used to characterize the regeneration of wound tissue. As seen in Fig. 6F, compared with other groups, epithelialization of the wounds of mice treated with CHA@GOx can clearly be seen 7 days after treatment, and this epithelialization began to thin by 14 days after treatment. This suggests that the epithelium was completely formed in these animals by Day 14. This conclusion is consistent with the epithelial thickness calculated with ImageJ software (Fig. S17). Next, the production of collagen in the tissue was evaluated. From the results of Masson's trichrome staining shown in Fig. 6G, CHA@GOx promoted the formation of collagen in the early stages of wound healing, and this collagen gradually matured and settled by 14 days after treatment. This process marks an orderly remodeling stage. The formation of collagen in mice treated with CHA lagged behind that of the CHA@GOx mice, but the mice treated with PBS experienced the slowest collagen formation process. To further characterize the collagen that was formed, Picrosirius red staining was used to selectively stain mature type I collagen in red or orange and new type III collagen in green. The results of collagen typing by Picrosirius red staining are shown in Fig. 7A and B, and they were consistent with the results of Masson's trichrome staining. Specifically, at 14 days posttreatment, orange–red mature type I collagen was observed in the wounds of mice treated with CHA@GOx, while in mice treated with PBS or CHA, green nascent type III collagen was observed at 14 days and 7 days, respectively.

The formation of local new blood vessels is a key factor in accelerating the healing of diabetic wounds. Therefore, anti-CD31 staining was used

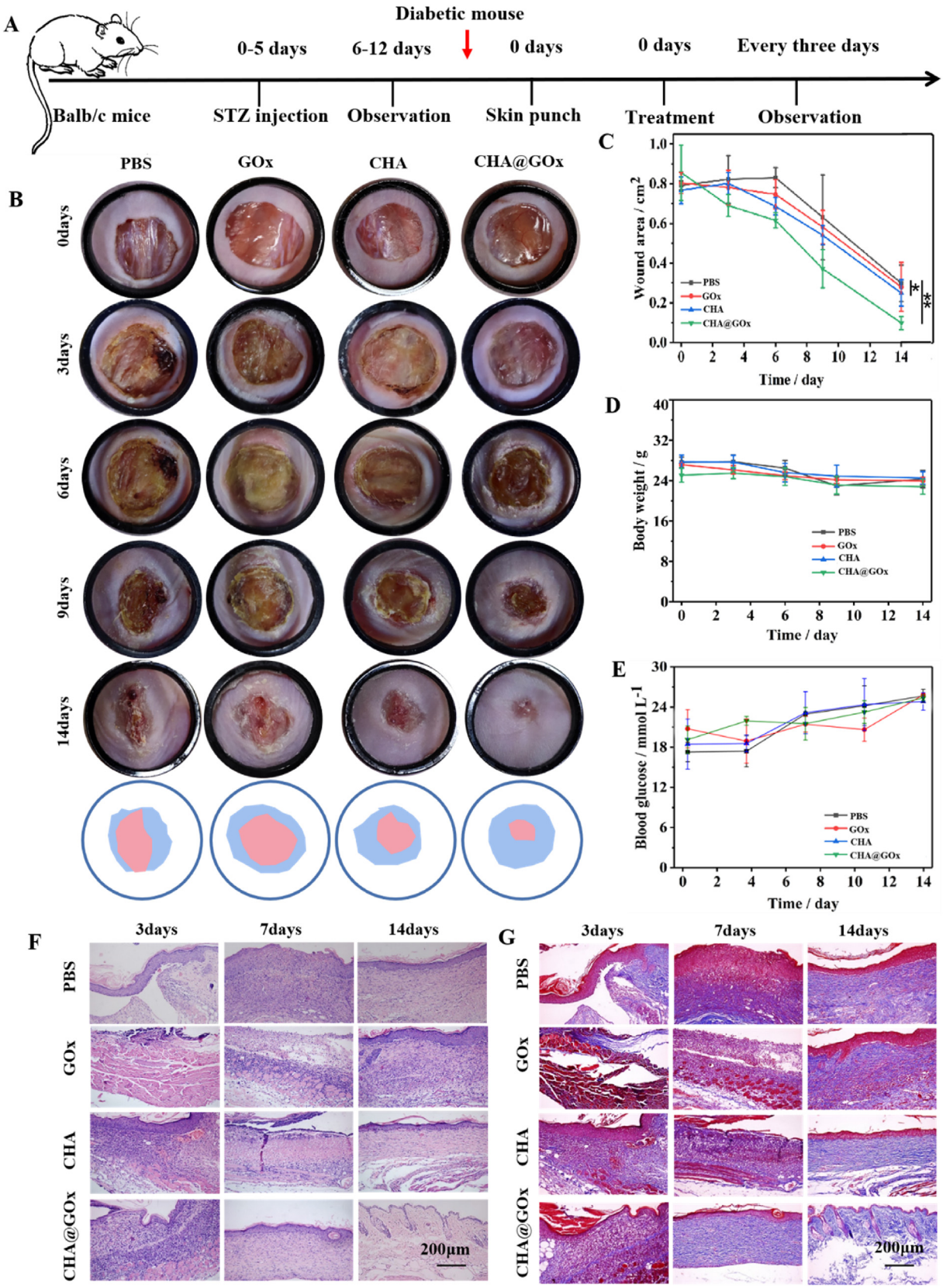

Fig. 6. *In vivo* diabetic wound healing studies. A) Schematic diagram of diabetic mice and wound model establishment. B) Representative images of wounds in diabetic mice within two weeks. C-E) Records of wound area, body weight and blood glucose of diabetic mice in two weeks. F) H&E staining of diabetic wound tissue on different days (3, 7,14 days) to measure epithelialization. G) Masson's trichrome staining of diabetic wound tissue on different days (3, 7,14 days) to measure collagen deposition.

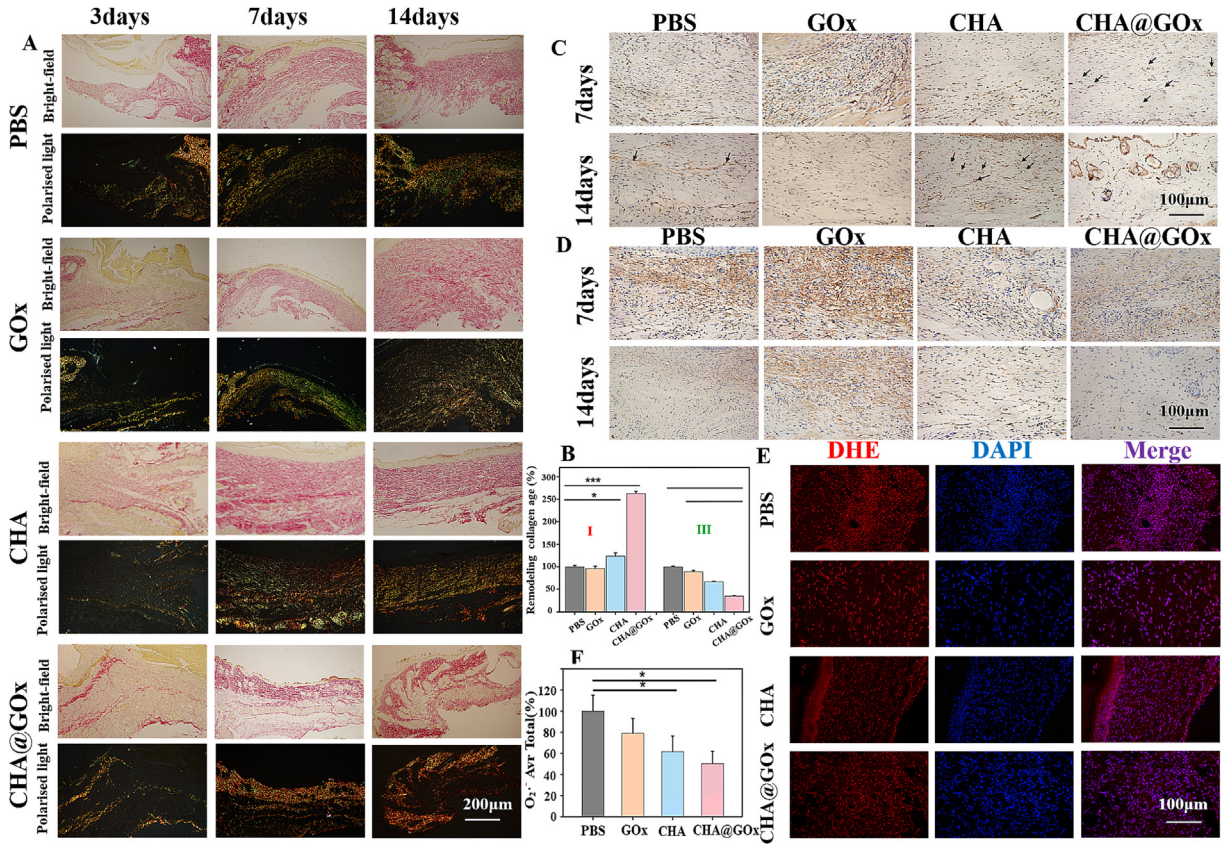

Fig. 7. Histological and immunohistochemical analysis of wound. A) Picrosirius red staining of diabetic wound tissue on different days (3, 7,14days) to Collagen typing, Collagen I (Red), Collagen III (Green). B) Quantify Collagen I and Collagen III of diabetic wound tissue at 14 days by Image J software. C) CD31 staining of diabetic wound tissue on different days (Day 7 and Day 14) to measure angiogenesis. D) α-SMA staining of diabetic wound tissue on different days (Day 7 and Day 14) to assess wound healing. E) DHE staining of diabetic wound tissue at 14 days to measure superoxide radical. F) Quantify superoxide radical of diabetic wound tissue at 14 days by ImageJ software.

to count the neovascularization of the wound. As shown in Fig. 7C, the formation of new blood vessels was observed 7 and 14 days after treatment with CHA@GOx and CHA, respectively. However, during this period, less angiogenesis was observed in mice treated with PBS. What is even more interesting is that on Day 14, hair follicles appeared in the wound tissues of the CHA@GOx group, this observation is important because hair follicles can differentiate into the epidermis and contribute to re-epithelialization in the process of skin wound healing [63]. These results can be attributed to the remodeled wound microenvironment and the inherent upregulation of angiogenic factor (VEGF) expression in ceria nanoparticles [64].

The presence of α-smooth muscle actin (α-SMA) is widely regarded as another sign of skin healing in the middle and late stages, but overexpression of this protein may cause malignant healing of the skin, such as scars. As shown in Fig. 7D and Fig. S18, we investigated the expression of α-SMA by staining tissue sections with an anti-α-SMA antibody. During the treatment process, it was clearly observed that the expression of α-SMA in the CHA@GOx group was higher than that in the PBS group on the 7th day, which was mainly due to the promotion of wound healing by CHA@GOx. By the 14th day, the α-SMA expression of CHA@GOx began to decrease as its healing reached the end stage, while the α-SMA expression of the PBS group increased significantly, suggesting that the repair stage was significantly lagging behind that of the CHA@GOx group. Alternatively, there may have been malignant healing.

Finally, the superoxide levels in wound tissues were quantified with dihydroethidine (DHE) on day 14 posttreatment. As shown in Fig. 7E - F, the fluorescence of both the CHA group and the CHA@GOx group was significantly reduced, suggesting that their SOD-like activity scavenges superoxide anions from the wound surface. This corresponds to the ability of CHA@GOx to scavenge excess ROS. Together, these histological and immunostaining results suggest that CHA@GOx can effectively promote the healing of diabetic wounds by promoting skin epithelialization, collagen deposition blood vessel and hair follicle production while regulating the level of α-SMA and removing excess ROS.

4. Conclusion

In this study, we developed and evaluated multifunctional nanozymes that regulate the microenvironment of diabetic wounds. Conceptually, CHA@GOx is endowed with abundant SOD, CAT and GOx activities due to the dynamic balance of the redox valence states on the surface of the cerium ions, which is the key to removing excess glucose and ROS and regulating the oxygen balance of the system. As evidence, we indicate that compared with the untreated hyperglycemia group, the CHA@GOx group has a significant effect in promoting diabetic wound healing, providing a promising method for the treatment and management of chronic diabetic wounds.

Credit author statement

Xiaojuan Yu and Xiaoxue Fu prepared the nanozyme CHA@GOx and completed the characterization analysis. Xiaojuan Yu was in charge of all cytology-related experiments, and Xiaojuan Yu, Jiaxin Yang and Lu Chen completed animal experiments and histopathological examinations. Yu Xiaojuan, Fu Xiaoxue and Leng Feng completed the writing of the article.

Declaration of competing interest

The authors declare that they have no known competing financial interests or personal relationships that could have appeared to influence the work reported in this paper.

Acknowledgements

This work was financially supported by National Natural Science Foundation of China (No. 81703156), Chongqing special project for technological innovation and application development (cstc2020jscx-msxmX0070) and Youth Talent Foundation in College of Pharmacy, China, Chongqing, Chongqing Medical University (No. YXY2019QNGD1).

Appendix A. Supplementary data

Supplementary data to this article can be found online at https://doi.org/10.1016/j.mtbio.2022.100308.

References

[1] H. King, R.E. Aubert, W.H.J.D.C. Herman, Global burden of diabetes, 1995–2025: prevalence, numerical estimates, and projections, Diabetes Care 21 (1998) 1414.
[2] S. Wild, G. Roglic, A. Green, R. Sicree, H.J.D.C. King, Global prevalence of diabetes, Diabetes Care 27 (2004) 1047–1053.
[3] Y. Yang, H.J.C.M. Jian, New progress on treatment for chronic ulcer of diabetic foot, Chongqing Med. J. 32 (2019) 832–837.
[4] J. Yang, W.N. Zeng, P. Xu, X. Fu, X. Yu, L. Chen, F. Leng, C. Yu, Z. Yang, Glucose-responsive multifunctional metal–organic drug-loaded hydrogel for diabetic wound healing, Acta Biomater. 140 (2021) 206–218.
[5] A.E. Kitabchi, G.E. Umpierrez, M.B. Murphy, E.J. Barrett, R.A. Kreisberg, J.I. Malone, B.M.J.D.c. Wall, Management of hyperglycemic crises in patients with diabetes, Diabetes Care 24 (2001) 131–153.
[6] H. Sano, S. Ichioka, Influence of oxygen on wound healing dynamics in healing-impaired diabetic mice, J. Plast. Surg. Hand Surg. 49 (2015) 135–140.
[7] Sergiu-Bogdan, Xiaowei Catrina, Z.J.D.M. Research, Reviews, Disturbed hypoxic responses as a pathogenic mechanism of diabetic foot ulcers, Diabetes Metab. Res. Rev. 32 (2016) 179–185.
[8] Y. Qian, C. Xu, W. Xiong, N. Jiang, J. Shen, Dual cross-linked organic-inorganic hybrid hydrogels accelerate diabetic skin wound healing, Chem. Eng. J. 417 (2021), 129335.
[9] A. Das, V. Govindasamy, Understanding the multifaceted mechanisms of diabetic wound healing and therapeutic application of stem cells conditioned medium in the healing process, J. Tissue Eng. Regen. Med. 13 (2019) 2218–2233.
[10] H. Wu, F. Li, W. Shao, J. Gao, D.J.A.C.S. Ling, Promoting angiogenesis in oxidative diabetic wound microenvironment using a nanozyme-reinforced self-protecting hydrogel, ACS Cent. Sci. 5 (2019) 477–485.
[11] X. Qi, Y. Xiang, E. Cai, S. You, G.L.D.L.H. Shen, All-in-one: harnessing multifunctional injectable natural hydrogels for ordered therapy of bacteria-infected diabetic wounds, Chem. Eng. J. 439 (2022), 135691.
[12] Y. Wang, T. Ying, J. Li, Y. Xu, W.K.S.X.L. Lin, KailiHierarchical micro/nanofibrous scaffolds incorporated with curcumin and zinc ion eutectic metal organic frameworks for enhanced diabetic wound healing via anti-oxidant and anti-inflammatory activities, Chem. Eng. J. 402 (2020), 126273.
[13] Mehran Haidari, Zhang Wei, James Willerson, J.C. Diabetology, Disruption of endothelial adherens junctions by high glucose is mediated by protein kinase C-β–dependent vascular endothelial cadherin tyrosine phosphorylation, Cardiovasc. Diabetol. 16 (2017) 136.
[14] A. Ql, B. Kl, A. Yl, C. Hs, A. Jg, D. Qr, Z.A. Tian, D.B. Jing, A.J.M. Jx, The impact of hyperglycaemia on PKM2-mediated NLRP3 inflammasome/stress granule signalling in macrophages and its correlation with plaque vulnerability: an in vivo and in vitro study - ScienceDirect, Metabolism 107 (2020), 154231.
[15] A.E. Louiselle, S.M. Niemiec, C. Zgheib, K.W.J.T.R. Liechty, Macrophage polarization and diabetic wound healing, Transl. Res. 236 (2021) 109–116.
[16] A. Apv, A. Kh, A. As, A. Ads, Therapeutic strategies for enhancing angiogenesis in wound healing, Adv. Drug Deliv. Rev. 146 (2019) 97–125.
[17] K. Sada, T. Nishikawa, D. Kukidome, T. Yoshinaga, E.J.P.O. Araki, Hyperglycemia induces cellular hypoxia through production of mitochondrial ROS followed by suppression of aquaporin-1, PLoS One 11 (2016), e0158619.
[18] Y. Hao, W. Zhao, H. Zhang, W. Zheng, Q. Zhou, Carboxymethyl chitosan-based hydrogels containing fibroblast growth factors for triggering diabetic wound healing, Carbohydr. Polym. 287 (2022) 119336.
[19] R. Yu, Y. Yang, J. He, M. Li, B. Guo, Novel supramolecular self-healing silk fibroin-based hydrogel via host-guest interaction as wound dressing to enhance wound healing, Chem. Eng. J. 417 (2021), 128278.
[20] X. Zhang, G. Chen, Y. Liu, L. Sun, Y. Zhao, Black phosphorus-loaded separable microneedles as responsive oxygen delivery carriers for wound healing, ACS Nano 14 (2020) 5901–5908.
[21] H. Zhang, G. Chen, Y. Yu, J. Guo, Q. Y, Microfluidic printing of slippery textiles for medical drainage around wounds, Adv. Sci. 7 (2020), 2000789.
[22] Y. Wang, L. Shang, G. Chen, L. Sun, X. Y, Bioinspired structural color patch with anisotropic surface adhesion, Sci. Adv. 6 (2020), eaax8258.
[23] Y. Guan, H. Niu, Z. Liu, Y. Dang, J. M. L. J, Sustained oxygenation accelerates diabetic wound healing by promoting epithelialization and angiogenesis and decreasing inflammation, Sci. Adv. 7 (2021), eabj0153.
[24] Y. Qi, K. Qian, J. Chen, Y. Shi, H. L, A thermoreversible antibacterial zeolite-based nanoparticles loaded hydrogel promotes diabetic wound healing via detrimental factor neutralization and ROS scavenging, J. Nanobiotechnol. 19 (2021) 414.
[25] X. Zhao, L. Chang, Y. Hu, S. Xu, Z. X. X. Z, Preparation of photocatalytic and antibacterial MOF nanozyme used for infected diabetic wound healing, ACS Appl. Mater. Interfaces 14 (2022) 18194–18208.
[26] Y. Liang, Z. Li, Y. Huang, R. Yu, B. Guo, Dual-dynamic-bond cross-linked antibacterial adhesive hydrogel sealants with on-demand removability for post-wound-closure and infected wound healing, ACS Nano 15 (2021) 7078–7093.
[27] Y. Liang, M. Li, Y. Yang, L. Qiao, H. B, pH/glucose dual responsive metformin release hydrogel dressings with adhesion and self-healing via dual-dynamic bonding for athletic diabetic foot wound healing, ACS Nano 16 (2022) 3194–3207.
[28] Y. Zhang, P. Zhang, X. Gao, L. Chang, Z. X, Preparation of exosomes encapsulated nanohydrogel for accelerating wound healing of diabetic rats by promoting angiogenesis, Mater. Sci. Eng. C Mater. Biol. Appl. 120 (2021), 111671.
[29] Y. Zhu, J. Zhang, J. Song, J. Yang, Z. Du, W. Zhao, H. Guo, C. Wen, Q. Li, X.J.A.F.M. Sui, A multifunctional pro-healing zwitterionic hydrogel for simultaneous optical monitoring of pH and glucose in diabetic wound treatment, Adv. Funct. Mater. 30 (2020), 1905493.
[30] X. Liu, Z. Yan, Z. Zhang, Y. Sun, R.J, Two-dimensional metal-organic framework/enzyme hybrid nanocatalyst as a benign and self-activated cascade reagent for in vivo wound healing, ACS Nano 13 (2019) 5222–5230.
[31] B. Halliwell, M. Whiteman, Measuring reactive species and oxidative damage in vivo and in cell culture: how should you do it and what do the results mean? Br. J. Pharmacol. 142 (2010) 231–255.
[32] W.D.G.J.P. Reviews, Free radicals in the physiological control of cell function, Physiol. Rev. 82 (2002) 47–95.
[33] R. Bonetta, Potential therapeutic applications of MnSODs and SOD-mimetics, Chemistry 24 (2017) 5032–5041.
[34] R.W. Gracy, J.M. Talent, Y. Kong, C.C.J.M.R. Conrad, Reactive oxygen species: the unavoidable environmental insult? Mutat. Res. 428 (1999) 17.
[35] M. Schieber, N.J.C.B. Chandel, ROS function in redox signaling and oxidative stress, Curr. Biol. 24 (2014) R453–R462.
[36] H. Zare, M. Rezayi, E. Aryan, Z. Meshkat, B. Hatmaluyi, A. Neshani, K. Ghazvini, M. Derakhshan, M.J.B. Sankian, A. Biochemistry, Nanotechnology-driven advances in the treatment of diabetic wounds, Biotechnol. Appl. Biochem. 68 (2021) 1281–1306.
[37] K.B. Narayanan, H.H. Park, Pleiotropic functions of antioxidant nanoparticles for longevity and medicine, Adv. Colloid Interface Sci. 201–202 (2013) 30–42.
[38] D.Y. Zhang, H. Liu, C. Li, M.R. Younis, P.J.A.A.M. Huang, Interfaces, ceria nanozymes with preferential renal uptake for acute kidney injury alleviation, ACS Appl. Mater. Interfaces 12 (2020) 56830–56838.
[39] C. Xu, X.J.N.A.M. Qu, Cerium oxide nanoparticle: a remarkably versatile rare earth nanomaterial for biological applications, NPG Asia Mater. 6 (2014) 102–108.
[40] R. Augustine, A. Hasan, N.K. Patan, Y.B. Dalvi, A.J.A.B.S. Moustafa, Engineering, cerium oxide nanoparticle incorporated electrospun poly(3-hydroxybutyrate- co -3-hydroxyvalerate) membranes for diabetic wound healing applications, ACS Biomater. Sci. Eng. 6 (2019) 58–70.
[41] Z. Xu, Y. Xu, P. Basuthakur, C.R. Patra, S. Ramakrishna, Y. Liu, V. Thomas, H.S. Nanda, Fibro-porous PLLA/gelatin composite membrane doped with cerium oxide nanoparticles as bioactive scaffolds for future angiogenesis, J. Mater. Chem. B 8 (2020) 9110–9120.
[42] R. Augustine, A.A. Zahid, A. Hasan, Y.B. Dalvi, J.J.A.B.S. Jacob, Engineering, cerium oxide nanoparticle-loaded gelatin methacryloyl hydrogel wound-healing patch with free radical scavenging activity, ACS Biomater. Sci. Eng. 7 (2020) 279–290.
[43] L. Zhou, W. Li, Y. Wen, X. Fu, Z.Y. Yang, Chem-inspired hollow ceria nanozymes with lysosome-target for tumor synergistic phototherapy, J. Mater. Chem. B 9 (2021) 2515–2523.
[44] C. Zhang, S. Hong, M. Liu, W.Y. Yu, M.K. Zhang, L. Zhang, X. Zeng, X.Z. Zhang, pH-sensitive MOF integrated with glucose oxidase for glucose-responsive insulin delivery, J. Contr. Release 320 (2020) 159–167.
[45] J. Cao, X. Li, H.J.C.M.C. Tian, Metal-organic framework (MOF)-Based drug delivery, Curr. Med. Chem. 27 (2020) 5949–5969.
[46] W. Sun, X. Li, C. Sun, Z. Huang, W.J.C. Shen, Insights into the pyrolysis processes of Ce-MOFs for preparing highly active catalysts of toluene combustion, Catalysts 9 (2019) 682.
[47] M. Motamedi, M. Ramezanzadeh, B. Ramezanzadeh, M. Mahdavian, One-pot synthesis and construction of a high performance metal-organic structured nano pigment based on nanoceria decorated cerium (III)-imidazole network (NC/CIN) for effective epoxy composite coating anti-corrosion and thermo-mechanical properties improvement, Chem. Eng. J. 382 (2020), 122820.
[48] X. Wenlong, Z. Yueping, L. Hongfei, L.J.M. Chang-Jun, Nanoparticle/metal–organic framework composites for catalytic applications: current status and perspective, Molecules 22 (2017) 2103.
[49] Z.Y. Yang, S.L. Luo, H. Li, S.W. Dong, X.C.J.R.A. Yang, Alendronate as a robust anchor for ceria nanoparticle surface coating: facile binding and improved biological properties, RSC Adv. 4 (2014) 59965–59969.

[50] J. Dolai, K. Mandal, N.R. Jana, Nanoparticle size effects in biomedical applications, ACS Appl. Nano Mater. 4 (2021) 6471–6496.
[51] Y. Feng, Y. Zhao, J.J.A.C.A. Ge, Impact of the size effect on enzymatic electrochemical detection based on metal-organic frameworks, Anal. Chim. Acta 1149 (2021), 238191.
[52] S. Amjad, M.J.M. Serajuddin, C.o.D.D. Systems, Nanoparticle drug delivery: an advanced approach for highly competent and multifunctional therapeutic treatment, Drug Deliv. Trans. Res. (2021) 183–193.
[53] S. Saghazadeh, C. Rinoldi, M. Schot, S.S. Kashaf, A. Khademhosseini, Drug delivery systems and materials for wound healing applications, Adv. Drug Deliv. Rev. 127 (2018) 138–166.
[54] N. Yadav, S.J.I.C. Singh, Polyoxometalate-mediated vacancy-engineered cerium oxide nanoparticles exhibiting controlled biological enzyme-mimicking activities, Inorg. Chem. 60 (2021) 7475–7489.
[55] T. Pirmohamed, J.M. Dowding, S. Singh, B. Wasserman, E. Heckert, A.S. Karakoti, J. King, S. Seal, W.T.J.C.C. Self, Nanoceria exhibit redox state-dependent catalase mimetic activity, Chem. Commun. 46 (2010) 2736–2738.
[56] P. Yang, Z. Zhu, T. Zhang, W. Zhang, X.J.S. Zhou, Orange-emissive carbon quantum dots: toward application in wound pH monitoring based on colorimetric and fluorescent changing, Small 15 (2019), 1902823.
[57] A.R. Pecoraro, B.D. Hosfield, H. Li, W.C. Shelley, T.A.J.S. Markel, Angiogenesis: a cellular response to traumatic injury, publish ahead of print, Shock 55 (2021) 301–310.
[58] F.B.R.d.M.a. b, B.A.F. A, E.H.M. A, A.B.J. C, A.G.S. D, R.D.A.S. A, J.A.L.G. c, R.I.M.d.A.R. d, D.L.R. A, F.d.A.A. a, Topic use of Annona crassiflora Mart. contributes to wound healing due to the antioxidant and proliferative effects of fibroblasts, Injury 53 (2021) 844–857.
[59] C. Marziano, G. Genet, K.K.J.A. Hirschi, Vascular endothelial cell specification in health and disease, Angiogenesis 24 (2021) 213–236.
[60] E. Kerr, D.J. Hayne, L.C. Soulsby, J.C. Bawden, S.J. Blom, E.H. Doeven, L.C. Henderson, C.F. Hogan, P.S. Francis, A redox-mediator pathway for enhanced multi-colour electrochemiluminescence in aqueous solution, Chem. Sci. 13 (2022) 469–477.
[61] T. Soydas, M. Sayitoglu, E.Y. Sarac, S. Cnar, G.K. Sultuybek, Biochemistry, Metformin reverses the effects of high glucose on human dermal fibroblasts of aged skin via downregulating RELA/p65 expression, J. Physiol. Biochem. 77 (2021) 443–450.
[62] N. Raina, R. Rani, M.J.E.S.i.V.D, Gupta, disease, angiogenesis: aspects in wound healing, Arterioscler. Thromb. Vasc. Biol. (2021) 77–90.
[63] Lay Kenneth, Tsutomu Kume, Elaine, F.J.P.o.t.N.A.o.S.o.t.U.S.o, America, FOXC1 maintains the hair follicle stem cell niche and governs stem cell quiescence to preserve long-term tissue-regenerating potential, Proc. Natl. Acad. Sci. U. S. A. 113 (2016) E1506–E1515.
[64] J. Xiang, J. Li, J. He, X. Tang, C. Z. B. C. F. L. S. X, Cerium oxide nanoparticle modified scaffold interface enhances vascularization of bone grafts by activating calcium channel of mesenchymal stem cells, ACS Appl. Mater. Interfaces 8 (2016) 4489–4499.